ARTICLE

Check for updates
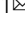
Focused surface plasmon polaritons coherently couple to electronic states in above-threshold electron emission

Pascal Dreher [1✉], David Janoschka [1], Bettina Frank[2], Harald Giessen [2] & Frank-J. Meyer zu Heringdorf[1,3]

When an intense light field strongly interacts with the band structure of a solid, the formation of hybrid light-matter quantum states becomes possible. Examples of such Floquet-Bloch states have been reported, but engineering of the band structure using Floquet states can suffer from dissipation and decoherence. Sustaining the necessary quantum coherence of the light-matter interactions requires robust electronic states in combination with strong fields of suitable polarization and frequency. Here, we explore the quantum coherent coupling of nano-focused surface plasmon polaritons (SPP) to distinct electronic states in the band structure of a solid. We observe above-threshold electron emission from the Au(111) Shockley surface state by the absorption of up to seven SPP quanta. Using time-resolved photoelectron spectroscopy the coherence of the interaction of the SPPs with the surface state during electron emission is investigated and the process is shown to be similar to light-driven above threshold electron emission. Ultimately, our work could render SPP-based Floquet engineering in nano-optical systems feasible.

---

[1] Faculty of Physics and Center for Nanointegration Duisburg-Essen (CENIDE), University of Duisburg-Essen, 47048 Duisburg, Germany. [2] 4th Physics Institute, Research Center SCoPE, and Integrated Quantum Science and Technology Center, University of Stuttgart, 70569 Stuttgart, Germany. [3] Interdisciplinary Center for the Analytics on the Nanoscale (ICAN), 47057 Duisburg, Germany. ✉email: pascal.dreher@uni-due.de

The coherent periodic driving of the electronic degrees of freedom of matter using intense light fields provides a route to realize exotic material properties that do not exist under equilibrium conditions[1–3]. Floquet theory predicts that such periodic driving can modify the original electronic structure by the formation of light-dressed electron states (Floquet states)[4,5]. Accordingly, hybrid Floquet-Bloch states in solid state systems could be utilized to engineer the band structure and band topology of materials – a concept that is often referred to as Floquet engineering[6–11].

While Floquet phenomena have been extensively studied in idealized model systems in atomic optical lattices[12], scattering of electrons intrinsically limits the applicability of the Floquet picture when solid state systems are concerned[13,14]. To realize Floquet-Bloch states in solids, the interaction with the driving field needs to dominate over dissipation and decoherence and thus robust electronic states in combination with strong fields with suitable polarization and driving period are needed[15,16]. Hence, only few experimental realizations of Floquet-Bloch states have been accomplished. Using laser-based time- and angle-resolved photoemission spectroscopy (ARPES), Floquet-Bloch states were demonstrated using topological surface states[17,18], in transition metal dichalcogenides[15], and on noble metal surfaces[19]. Furthermore, the opening of a topological band-gap by the formation of Floquet-Bloch states has been demonstrated using anomalous Hall currents in graphene[20].

In nano-optical systems electromagnetic fields are controlled with sub-wavelength and sub-period precision, which makes them ideal candidates to realize Floquet-Bloch states[21–24]. The tremendous enhancement of local field amplitudes by surface plasmon resonances in nano-optical systems can trigger strong-field light-matter interactions[25], including highly nonlinear electron emission[26–30] even at low-power continuous-wave excitation[31], or the generation of high-harmonic radiation[32]. To further increase the local field strength, propagating surface plasmon polaritons (SPPs) can be focused, for example, using nano-tips[33–36], Fresnel lenses[37], circular lenses[29,38,39], metalenses[40], or plasmonic orbital angular momentum (OAM)[41] like in Archimedean spirals[42,43].

However, the coherent coupling of SPPs to distinct electronic states in the band structure of a solid during nonlinear electron emission in the absence of light – a prerequisite for the formation and observation of SPP-induced Floquet-Bloch states – has so far not been investigated. Here, we explore nano-focusing of femtosecond SPP pulses in Archimedean spirals as a possible route for creating the fields that are necessary for strong-field control over electronic states within a solid. We observe nonlinear electron emission from the Au(111) Shockley surface state (SS) by the absorption of up to seven SPP quanta by employing spatially-selective angle-resolved electron spectroscopy at the SPP nano-focus. Two-dimensional interferometric time-resolved photoelectron spectroscopy[44] provides us with direct access to the coherent and incoherent dynamics of the electron emission process in the SPP nano-focus. Our results clearly indicate the quantum coherent nature of the interaction of the intense SPP nano-focus with the band structure of the material during above-threshold electron emission. Ultimately, our work indicates that SPP-based above-threshold electron emission is not different from light-based approaches and might be utilized to realize SPP-based Floquet engineering.

Results and discussion
Surface plasmon polariton nano-focusing for deep-subwavelength probing volumes. To observe the coherent coupling of SPPs to distinct electronic states in the band structure

during electron emission, the energy and momentum of the emitted electrons need to be resolved, while only the electrons that originate from the SPP nano-focus are detected. The experiments are therefore performed in a spectroscopic photo-emission and low energy electron microscope (SPELEEM)[45] equipped with a hemispherical energy filter (Fig. 1a). The required spatial selectivity of the electron detection is provided by an aperture in a conjugate image plane in the center of the sector.

We use nano-focusing of SPPs in Archimedean spirals, like the one shown in the scanning electron micrograph in Fig. 1b. The spiral was cut into the atomically flat (111) top-facet of a thermolytically grown self-organized Au-microplatelet[46,47] using focused ion beam milling (FIB). After cleaning of such samples within the ultra-high vacuum of the microscope (see Methods section), we routinely observe the $(22 \times \sqrt{3})$-superstructure of the clean Au(111) surface[48] in microprobe low-energy electron diffraction (Fig. 1c), corroborating the high crystalline quality of our samples.

On the sample, femtosecond SPP pulses are resonantly excited at the spiral using circularly polarized femtosecond laser pulses from a Ti:Sapphire oscillator with a central excitation energy of $\hbar\omega = 1.52$ eV in a normal-incidence geometry[49]. The spiral consists of a single groove that completes six revolutions around the spiral center to maximize the SPP excitation efficiency while maintaining a short SPP pulse duration[50]. With each revolution, the radius of the spiral decreases by the SPP wavelength $\lambda_{SPP} \approx 800$ nm, corresponding to a topological charge of the spiral of $L = -1$. This topological charge is compensated by using light with a spin angular momentum of $S = 1$ to yield an SPP pulse with vanishing OAM $J = L + S = 0$, i.e., by choosing the helicity of the incident circularly polarized light to be opposite to the helicity of the spiral[43]. The resulting vectorial electric field distribution just above the surface in the center of the spiral can be calculated analytically[43,51] and is plotted in Fig. 1d. The field in the focus is dominated by its out-of-plane component, which follows the zeroth-order Bessel function $E_z(r) \propto J_0(k_{SPP}r)$, with $k_{SPP} = 2\pi/\lambda_{SPP}$ for the SPP wavenumber. The isolated and azimuthally symmetric SPP nano-focus in the center of the spiral has a theoretical full width at half maximum (FWHM) of 387 nm, which is smaller than half the SPP wavelength.

Using the spectroscopic photoemission electron microscopy (PEEM) capabilities of the SPELEEM, we experimentally verify the focusing performance of the Archimedean spiral by imaging the spatial distribution of the nonlinear electron emission from the center of the spiral (Fig. 1e). Since at least 4 SPP quanta with $\hbar\omega = 1.52$ eV are required to overcome the work function of $\phi \approx 5.3$ eV of the clean Au(111) surface[52], the electron emission from the SPP nano-focus must be dominated by a 4th order electron emission process. The pass energy in the energy-filtered PEEM image in Fig. 1e was chosen such that only the dominant 4th order electron emission was detected to minimize chromatic aberrations. The spatial distribution of the electron emission shows an isolated maximum at the center of the spiral, indicating that the liberated electrons predominantly originate from the strong out-of-plane component of the SPP nano-focus. Notably, by the time the SPP pulse has propagated from the perimeter of the spiral to its center (≈ 20 μm propagation length), the exciting laser pulse (<15 fs pulse duration) has already decayed and is thus not relevant for the nonlinear electron emission. To distinguish such electron emission triggered exclusively by the SPP pulse from conventional photoemission, the former is usually referred to as plasmoemission[29,50].

Considering the 4th order nonlinearity of the electron emission process, the spatial distribution of the PEEM signal is given by $Y_{4PPE}(r) \propto I_{SPP}(r)^4 \propto J_0(k_{SPP}r)^8$, where $I_{SPP}(r)$ is the spatially
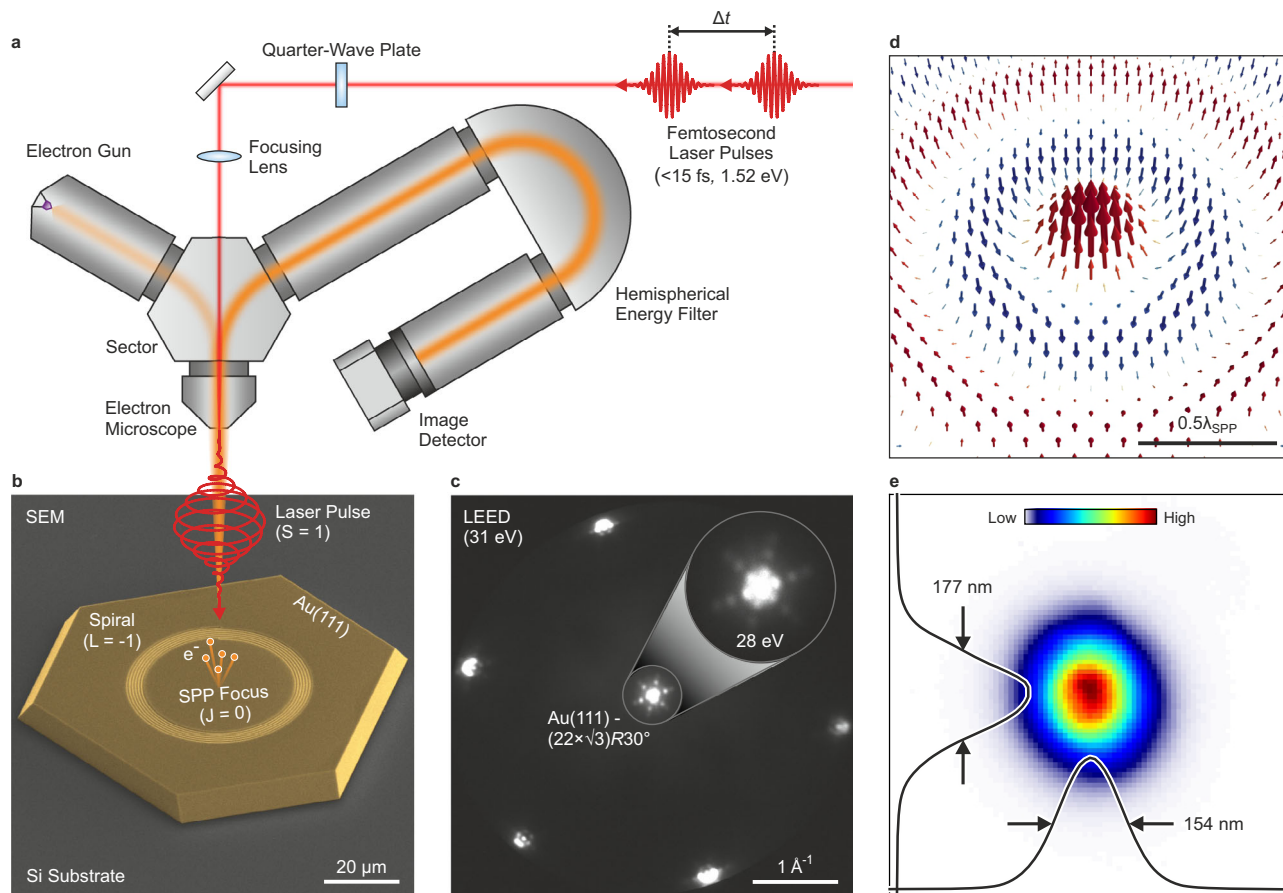
Fig. 1 Electron emission from nano-focused surface plasmon polariton pulses. a Sketch of the electron microscopy setup. Femtosecond laser pulses impinge on the sample surface along the surface normal. The emitted electrons are dispersed in an imaging energy filter and detected using a CMOS detector. **b** Scanning electron micrograph (SEM) of an Archimedean spiral like the ones used for the presented results. Upon excitation of the spiral with a circularly polarized laser pulse a surface plasmon polariton (SPP) nano-focus is formed in the center of the spiral. **c** Typical low-energy electron diffraction (LEED) pattern acquired after sample preparation in the microscope. **d** Plot of the calculated electric field vectors in the center of the Archimedean spiral. **e** Photoemission electron microscopy (PEEM) image of the spatial distribution of the photoelectrons that are emitted from the center of the Archimedean spiral in a linear false color scale (see color bar in panel **e**). The marginal distributions are plotted (black lines) and their respective full width at half maximum is indicated.

dependent intensity of the SPP field. We therefore expect that the FWHM of 387 nm of the electric field of the SPP nano-focus results in an electron emission maximum with an FWHM of 148 nm. This expectation is in excellent agreement with FWHMs extracted from the marginal distributions of the PEEM signal (black lines in Fig. 1e), which experimentally verifies the diffraction-limited focusing performance of the spiral. That higher-order side lobes from the J_0-like out-of-plane component are not observed is also due to the 4th order nonlinearity of the emission process, which suppresses emission from the first-order side lobe already by a factor of $\approx$1450 and higher-order side lobes by increasingly larger factors.

The extraordinary focusing performance of the spiral and the high nonlinearity of the electron emission process confine the electron emission such that laterally only a deep-subwavelength area of the sample surface is probed. In addition, the depth of the material that is accessible to the SPP's electric field is confined by the high nonlinearity of the emission process. The evanescent SPP electric field decays within the gold substrate with a decay constant of $z_m \approx 25.5$ nm. Because of the nonlinearity, the electron emission probability scales as $Y_{4PPE}(z) \propto I_{SPP}(z)^4 \propto \exp(-z/z_m)^8$, such that the effective decay length is reduced to $z_m/8 \approx 3.2$ nm. Remarkably, this depth corresponds to less than 5 atomic layers of the Au(111)

surface and is comparable to typical inelastic mean-free paths of low energy photoelectrons.

Coupling of surface plasmon polaritons to electronic bands during electron emission. We will now use the nonlinear electron emission from the presented SPP nano-focus to investigate the coupling of SPPs to distinct electronic states in a band structure. The (111) surface of the Au substrate is host to a prototypical Shockley surface state in its projected L-band gap, which recently has been classified as a topologically non-trivial surface state[53]. The pure out-of-plane polarization in its center makes the SPP nano-focus especially suited to investigate the coupling of the excited SPPs to that SS.

In the SPELEEM, the electrons from the SPP nano-focus are collected over the full solid angle in the vacuum half-space and dispersed in the imaging hemispherical energy filter. A slit in the exit plane of the energy filter in combination with imaging of the reciprocal plane provides us with momentum maps at constant final state energy. By applying a bias voltage to the sample relative to the analyzer potential, we vary the detected final state energy without varying the analyzer's pass energy or affecting the analyzer's energy resolution. This enables us to record the full three-dimensional angle-resolved electron spectrum from the SPP
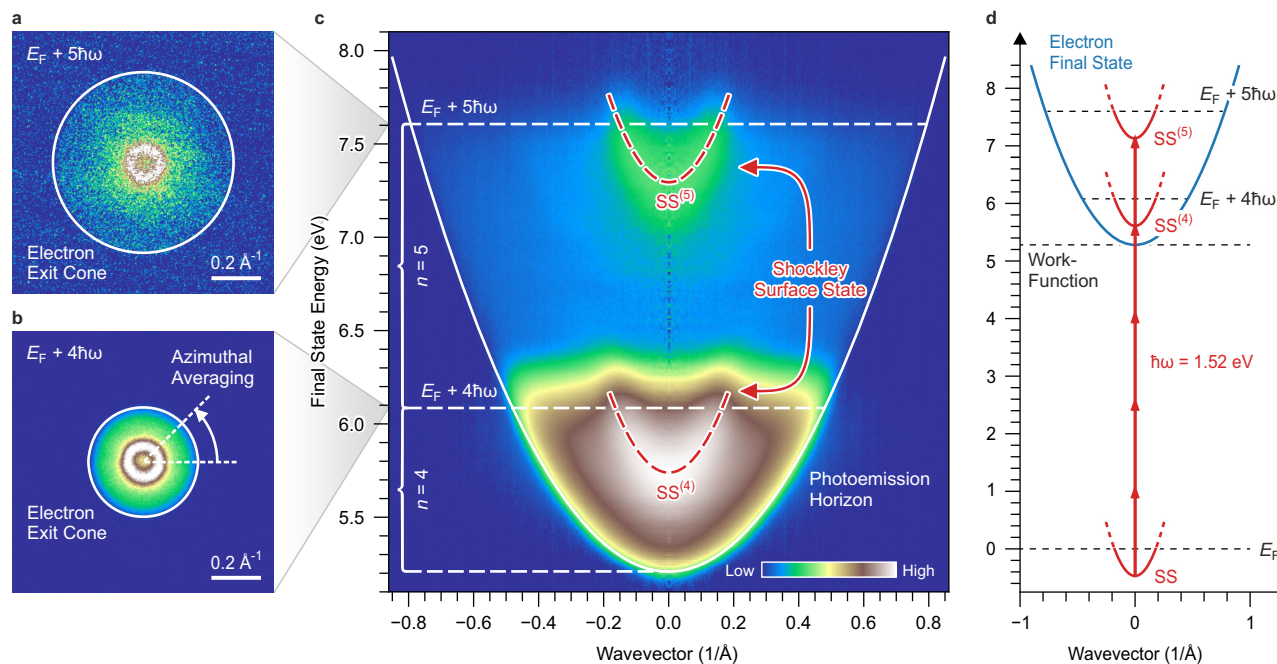
Fig. 2 Angle-resolved plasmoemission spectroscopy. a, b Momentum maps at $5\hbar\omega$ and $4\hbar\omega$ above the Fermi energy (E_F), corresponding to 4th ($n = 4$) and 5th ($n = 5$) order electron emission, respectively, with the photon energy $\hbar\omega = 1.52$ eV. The electron yield is depicted in a linear false color scale (see color bar in panel **c**). **c** Angle-resolved plasmoemission spectrum extracted from the full three-dimensional data stack via azimuthal averaging. The data is presented in a logarithmic false color scale (see color bar in panel **c**). The Shockley surface state (SS) is visible in 4th (SS$^{(4)}$) and 5th (SS$^{(5)}$) order electron emission. **d** Sketch of the electron emission process.

nano-focus, which we refer to as angle-resolved plasmoemission spectroscopy (ARPLES) in the remainder of this work.

Figure 2a, b show exemplary momentum maps at final state energies $5\hbar\omega$ and $4\hbar\omega$ above the Fermi energy, respectively. The electron emission appears to be almost perfectly symmetric around the Γ-point of the surface Brillouin zone (SBZ), as one would expect from the out-of-plane SPP polarization and the Au(111) surface band structure[53–55]. Azimuthal averaging of the three-dimensional dataset enabled by this symmetry leaves us with the ARPLES spectrum as a function of in-plane momentum (Fig. 2c). The quantal excitation ladder from the SS into the vacuum is sketched in Fig. 2d. Note, that in Fig. 2d the SPP absorption is symbolized by vertical arrows, i.e., the SPP's momentum is neglected, just like it is usually done for light-driven electron emission at optical energies. This approximation is justified by the fact that at $\hbar\omega = 1.52$ eV both the momentum of the SPP of $<10^{-3}$ Å^{-1} as well as the difference between the photon and the SPP momentum of $<10^{-5}$ Å^{-1} are negligible compared to the electron momenta considered in Fig. 2a–c. Accordingly, no evidence for effects caused by a finite SPP momentum is found in the data presented in Fig. 2a–c.

The ARPLES spectrum (Fig. 2c) is dominated by two parabolic features close to the Γ-point (red lines labeled SS$^{(4)}$ and SS$^{(5)}$), which appear as ring-like features in the momentum maps (Fig. 2a, b). Considering that the absorption of at least 4 SPP quanta is required to overcome the work function of the Au(111) surface, we must attribute the energetically lower-lying feature (SS$^{(4)}$) to 4th order electron emission from the SS. The parabolic feature appearing at higher final state energy (SS$^{(5)}$) must be attributed to 5th order above-threshold electron emission, as it is located exactly one SPP quantum $\hbar\omega$ above the SS$^{(4)}$ feature. Similarly, the Fermi edge is replicated in 4th and 5th order electron emission. In 5th order emission, however, the accessible in-plane momentum range is significantly larger compared to 4th order emission. This advantage has recently been proposed as a

technique to access states in the SBZ outside of the lowest-order photoemission horizon[56].

A second, independent determination of the orders of the electron emission processes can be obtained by measuring the power-law behavior of the electron yield for each feature as a function of the incident laser power (see Supplementary Note 1)[29]. That the SS$^{(4)}$ and SS$^{(5)}$ features indeed originate from the SS is verified by fitting the parabolic dispersion of these features in the ARPLES spectrum. The extracted effective mass of the SS is in reasonable agreement with previous studies performed using conventional ARPES (see Supplementary Note 2).

Coherence of the electron emission process probed by interferometric time-resolved plasmoemission spectroscopy. The results in Fig. 2 demonstrate that SPPs couple to distinct electronic states in the band structure of a solid, using 4th order near-threshold electron emission and 5th order above-threshold electron emission from the Au(111) surface state. Comparable experiments with optical excitation have recently shown that if light is used to excite above-threshold electron emission from noble metal surfaces, the emission process must be considered a single quantum coherent one-step nonlinear process[44,57]. In the case of intense SPP fields, it is questionable whether nonlinear electron emission similarly is a quantum coherent one-step process or if the coherence is lost along the nonlinear quantal excitation ladder: SPPs are collective excitations of the electron system at the surface and their collapse into individual emitted electrons is intrinsically a many-body scattering process. Recently, the collapse of bulk plasmons into individual electrons during photoemission has been demonstrated[58,59] and at least the quantum state of the bulk plasmon excitation has been described as being partially coherent. Still, it is unclear whether electron emission involving collective excitations such as SPPs or bulk plasmons in sum is a coherent or incoherent process, although
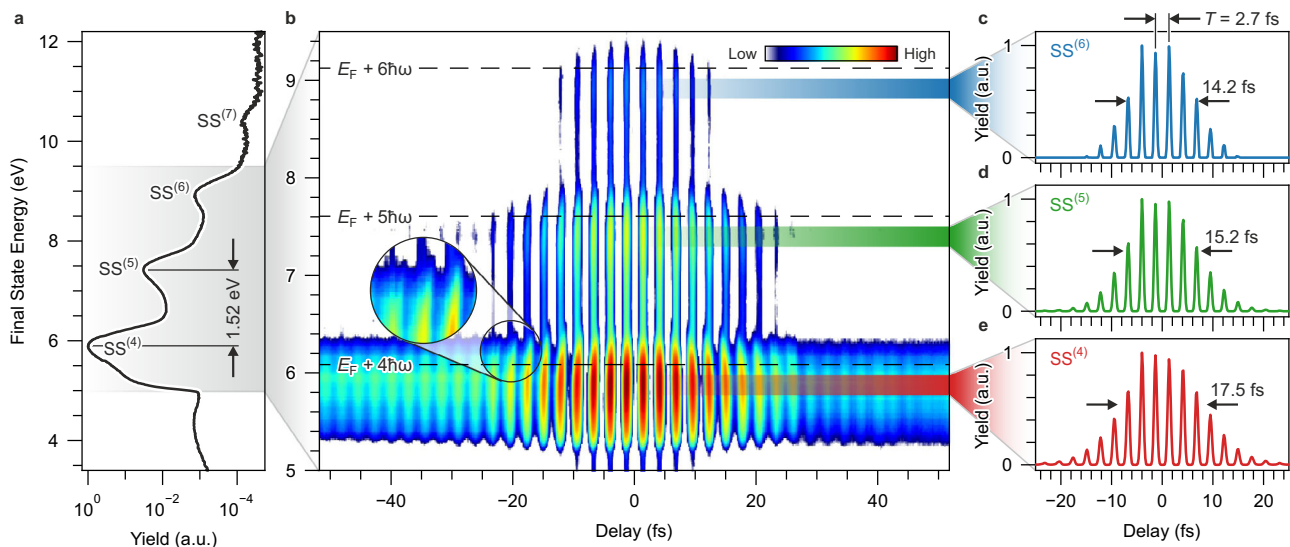
Fig. 3 Interferometric time-resolved plasmoemission spectroscopy. a High dynamic range electron spectrum showing up to 7th order above-threshold electron emission from the Shockley surface state (SS) on Au(111) triggered by a surface plasmon polariton (SPP) nano-focus in an Archimedean spiral. **b** Interferometric time-resolved plasmoemission spectra presented in a logarithmic false-color scale (see color bar in panel **b**) showing the dynamics of the electron emission process up to 6th order. The Fermi edges at $E_F + n\hbar\omega$ for the different electron emission orders n are indicated by the black dashed lines, where $\hbar\omega = 1.52$ eV is the SPP energy. **c–e** Line-profiles through the data in panel **b** extracted at the 6th to 4th order SS replica, respectively, by integration over an energy range of $\approx$200 meV for each peak. The arrows indicate the full widths at half maximum (FWHMs) of the envelopes of the line-profiles.

quantum coherence in these interactions would be essential for plasmonic Floquet engineering[15,16].

To probe the coherence of the observed SPP-driven electron emission, we performed interferometric time-resolved plasmoemission spectroscopy of the SPP nano-focus. We use interferometrically-stable phase-locked pairs of mutually delayed femtosecond laser pulses to excite SPP pulses instead of the single pulse excitation that was used for the results discussed above. Since the excitation of SPPs at an Archimedean spiral (Fig. 1b) is generally a linear process, the exciting laser pulse pairs directly result in equally interferometrically-stable phase-locked pairs of SPP pulses with the same mutual time delay. By scanning the time delay between the SPP pulses with sub-femtosecond precision we can track the coherent and incoherent dynamics of the electron emission process. Note, that by working in the dispersive plane of the analyzer we obtain an increased signal-to-noise ratio by partly integrating the electron spectrum over the emission angle at the cost of a slightly reduced energy resolution[45,60].

Figure 3a shows a typical plasmoemission spectrum acquired from the SPP nano-focus. In analogy to the ARPLES data (Fig. 2), we observe a peaked spectrum with a peak spacing that again matches the SPP energy of $\hbar\omega = 1.52$ eV. As the ARPLES spectrum was dominated by above-threshold emission from the SS of the Au(111) surface, the peaks in the spectrum in Fig. 3a must also correspond to above-threshold electron emission from that SS. Due to the improved detection, we are able to resolve above-threshold emission up to 7th order (SS$^{(7)}$ peak) in the spectrum in Fig. 3a. Considering that only a moderate-power Ti:Sapphire oscillator is used for the experiments, these results are indicative of the high nonlinearity of the interactions and the strong field-enhancement achieved in the SPP nano-focus. As a result of this strong field-enhancement, we detect electrons below the work-function cutoff of $\approx$5.3 eV[52] that could possibly reflect space-charge effects due to the high emission intensity in the SPP focus[61].

Interferometric time-resolved plasmoemission spectra are presented in Fig. 3b for a final state energy range covering the

SS$^{(4)}$ to SS$^{(6)}$ peaks. Generally, the data is dominated by interference fringes of the electron yield as a function of the time delay for all final state energies. The period duration $T \approx 2.7$ fs of the fringe oscillations matches the oscillation period of the SPP field amplitude. This can be understood by either considering the excitation of SPPs by the combined interfering laser pulses or equivalently by considering the interference of the SPP pulses that are excited by the individual laser pulses in each pulse pair. The two equivalent perspectives are due to the linearity of the excitation process, in which the superposition principle for the conversion of light into SPP fields needs to be fulfilled. If the exciting laser pulses are in-phase, the light intensity on the Archimedean spiral is maximal, which results in a maximal SPP intensity and thus maximal electron emission. In the equivalent picture, the SPP pulses that are excited by the individual in-phase laser pulses in each pulse pair also need to be in phase and interfere constructively, which again results in maximal SPP intensity and thus maximal electron emission. For out-of-phase laser pulses, the laser intensity on the Archimedean spiral is minimal and thus the excitation of SPP pulses is suppressed. In the equivalent picture, the SPPs excited by the individual out-of-phase laser pulses need to be out of phase as well such that the destructive interference of the individual SPP pulses results in minimal intensity and thus minimal electron emission in the nano-focus.

Since the electron yield is modulated by the interference of the fields, the temporal envelope of the electron yield needs to be dominated by the envelope of the pulses as well. We can use this to estimate a lower limit for the duration of the SPP pulse in the nano-focus. Figure 3c–e show time-dependent line-profiles through the data in Fig. 3b at the final state energies corresponding to the SS$^{(6)}$ to SS$^{(4)}$ peaks. The line-profiles resemble nth order autocorrelation functions, where the orders match the orders of the respective electron emission processes. The widths of the autocorrelation traces are anti-proportional to the emission orders as one would expect from conventional nonlinear autocorrelations of ultrashort laser pulses in nonlinear optics or photoemission. The full width at half maximum of the

autocorrelation traces $FWHM_{acorr}$ can be converted into durations of the SPP pulse intensity $FWHM_{SPP}$ by modelling the n-th order electron emission from the SS using an effective two-level system (see Supplementary Note 4). By combining the FWHMs from Fig. 3c–e, we extract an SPP pulse duration of $FWHM_{SPP}$ = (15.8 ± 0.3) fs. If compared to the laser pulse duration of <15 fs, the extracted SPP pulse duration indicates a minuscule pulse elongation induced by the response-function of the Archimedean spiral. The measured FWHM, however, also includes the electronic response of the Au(111) surface and is convoluted with associated lifetimes and coherence decay times of intermediate electronic states along the nth order excitation ladder[44,62–64]. For electron emission from the SS at the used SPP energy no real intermediate states are located in the projected surface band structure of the Au(111) substrate that could prolong the measured FWHM. Hence, the extracted number of $FWHM_{SPP}$ = (15.8 ± 0.3) fs is a direct measurement of the SPP pulse duration.

A closer inspection of the data in Fig. 3b reveals that in each emission order the interference fringes are slightly tilted (see, e.g., enlarged view of the encircled region in Fig. 3b). Such tilts are well known in interferometric frequency-resolved second harmonic generation, where they indicate a coherent nature of the underlying physical process[65,66]. In photoemission, such fringe tilts form the basis of coherent two-dimensional photoemission spectroscopy and are similarly interpreted: if coherence is not lost along the nth order excitation ladder of the photoemission process, the final state energy of a liberated photoelectron correlates with the frequency components that constitute the exciting laser pulse[44]. More specifically, if quanta from the higher energy end of the pulse spectrum are combined, the final state energy will be higher than if quanta from the lower energy end of the spectrum are combined. The oscillation frequency of the interference fringes varies accordingly and thus increases with higher final state energies.

The plasmoemission process is further analyzed in Fig. 4 by computing a Fourier transform of the data from Fig. 3b along the delay axis. Such analysis yields a two-dimensional plasmoemission spectrum (Fig. 4a) as a function of the final state energy on the y-axis and the modulation energy, i.e., the Fourier frequency, on the x-axis. For each emission order n, peaks at harmonics $m\hbar\omega$ of the fundamental SPP energy $\hbar\omega = 1.52$ eV are observed as a function of the modulation energy for $|m| \leq n$. Note that for emission orders $n > 4$ some of the higher order modulation energy peaks are not resolved as they are too close to the noise level.

All peaks in Fig. 4a are expected for Fourier transforms of autocorrelations from the nth order emission processes, even if scattering along the nth order excitation ladders destroyed the coherence. Whether the process is coherent or not is reflected in the detailed shapes of the peaks. This is discussed in the framework of Fig. 4b–e that show enlarged views of the $m = 1$ and $m = 3$ harmonics observed in the $n = 4$ and $n = 5$ electron emission peaks, respectively. In all these peaks we find a range of final-state energies where the modulation energy is fixed at the harmonic $m\hbar\omega$, indicating an incoherent electron emission process for these energies. The modulation energy, however, is only fixed for final state energies below the band minimum of the SS at ≈5.7 eV in the $n = 4$ case (Fig. 4b, c) and at ≈7.3 eV in the $n = 5$ case (Fig. 4d, e). Below the SS band minima the ARPLES spectrum in Fig. 2 only shows secondary electron emission backgrounds, making the absence of coherences (and energy correlations) plausible.

For final state energies involving electron emission from the SS, we find a correlation between the final state energy and the modulation energy. The slopes of the observed peaks
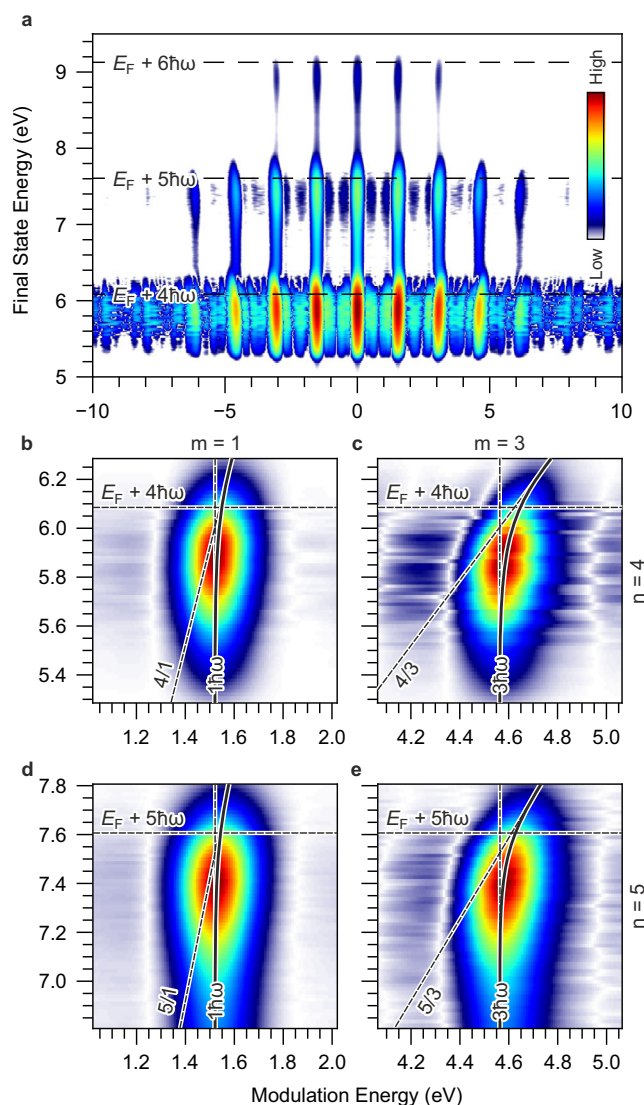
Fig. 4 Coherent two-dimensional plasmoemission spectroscopy.
a Coherent two-dimensional plasmoemission spectrum computed by a Fourier transform of the data in Fig. 3b along the delay axis, represented on a logarithmic false-color scale (see color bar in panel **a**). **b–e**, Enlarged views of different coherences in the electron emission process extracted from panel **c**, shown in a linear false-color scale (colors comparable to the color scale in panel **a**). **b**, **c** show the $m = 1$ and $m = 3$ coherences in 4th order electron emission ($n = 4$), whereas **d**, **e** show the same coherences in 5th order emission ($n = 5$). The tilts of the coherences match the expected asymptotic tilts starting from the position of the band minimum of the Shockley surface state (SS). The solid black lines indicate this behavior and are intended as guides to the eye.

asymptotically match the ratios m/n, where again m is the modulation energy harmonic and n is the order of the emission process.

Based on the same reasoning as in coherent two-dimensional photoemission spectroscopy[44], the observed correlations directly indicate that the nonlinear emission from the SS triggered by the intense SPP nano-focus needs to be interpreted as a quantum coherent one-step electron emission process. Only in this case the final state energies correlate linearly with the different frequency components in the SPP pulses and thus with the modulation energy, as observed by the fringe tilts in Fig. 3b and by the slopes

of the peaks in Fig. 4. Broadening, scattering, or dephasing along the nth order excitation ladder would make the initial state energy, the final state energy, and the modulation energy badly defined quantities. As a result, the observed correlations between the final state energy and the modulation energy would be lost, which is clearly not the case for emission from the SS.

Conclusions

We investigated the nature of the coupling of SPPs to distinct electronic states in the band structure of a solid, using the prototypical SS of the Au(111) surface as an example. The coupling of SPPs to the SS during nonlinear electron emission was identified by resolving the SS dispersion in ARPLES. In fact, the ARPLES spectrum in Fig. 2c appears to be similar to results obtained with conventional light-based above-threshold photoemission from the SS[67]. By performing interferometric time-resolved plasmoemission spectroscopy and analyzing the fringe structure of the electron yield[44], the emission process and thus the coupling of SPPs to the SS were determined to be of fully quantum coherent nature. In this sense, both the angle-resolved and time-resolved electron spectra reported in our work support the interpretation that SPP-driven electron emission is not different from conventional light-based above-threshold photoemission and can thus be described using standard above-threshold electron emission theories.

Strong SPP fields in combination with interferometric time-resolved plasmoemission spectroscopy are thus a promising candidate to possibly enable SPP-based dressing of electronic states and transitions, similar to the recent light-based experiments by Reutzel et al[19]. Compared to their work, the diffraction-limited nano-focusing of SPPs in an Archimedean spiral provides an extraordinary field-enhancement and nanoscopic spatial selectivity. Our approach could thus enable Floquet engineering already at low optical excitation intensities and on nanoscopic scales. To verify the existence of the therefore required SPP-induced Floquet-Bloch states it would be interesting to perform an SPP-pump UV-laser-probe photoelectron spectroscopy experiment, where the appearance of such states should be directly visible[18].

Our work forms the basis to study and manipulate the interaction of SPPs with more complicated band structures, such as SPP-based excitations of electrons in topological surface states[18] or in two-dimensional materials like graphene[20] and WSe$_2$[15]. The midinfrared excitation energies that are required for these materials are easily supported by surface plasmon resonances[27]. Furthermore, the general enhancement of strong-field light-matter interactions for these energies should appear advantageous for Floquet engineering. Extending our work to other polaritonic excitations, such as SPPs in the SS of topological insulators[68] or exciton-polaritons[69] and phonon-polaritons[70] in two-dimensional materials could make a broader class of materials accessible to Floquet engineering. Ultimately, our work provides a feasible route towards SPP-based Floquet engineering of electronic states in nanoscopic systems.

Methods

Experimental Setup. Archimedean spirals were milled into single-crystalline Au platelets[46] by focused ion-beam milling (FIB) either at the University of Duisburg-Essen using a FEI Helios NanoLab 600 equipped with a Ga ion-source, or at the University of Stuttgart using a Raith ionLINE Plus equipped with a Au ion-source. The inner diameter of the fabricated spirals was kept fixed at 40 μm while the depth of the spirals was kept in the range of 150 nm to 250 nm. The samples were transferred through air into a spectroscopic photoemission and low energy electron microscope (ELMITEC SPELEEM III)[45], where they were cleaned by oxygen plasma etching and several cycles of Argon ion sputtering and annealing at elevated temperature in ultra-high vacuum ($p < 10^{-10}$ mbar). The microscope is equipped

with a highly linear CMOS-based electron detector[71] (TVIPS TemCam F216), which enables high dynamic range imaging. An aperture in one of the conjugate image planes of the microscope is used to select only the electrons that originate from the studied SPP focus.

The microscope is combined with a Ti:Sapphire oscillator (Femtolasers Femtosource Compact) to excite SPP pulses and trigger the observed electron emission. Such combination of a photoemission microscope with an ultrafast laser setup has been established as a standard technique to investigate SPPs on their intrinsic energy, length, and time scales[72]. The used oscillator emits laser pulses with a pulse duration <15 fs and a central energy of $\hbar\omega = 1.52$ eV at a repetition rate of ≈80 MHz. For the time-resolved experiments, we used a Pancharatnam's phase stabilized Mach-Zehnder-interferometer[73,74] to create pairs of mutually delayed laser pulse pairs with sub-femtosecond stability and accuracy. The delay was tracked by recording the spectral interference of the laser pulses on a spectrometer (see Supplementary Note 3) and the time-dependent electron spectra were interpolated onto an equidistant delay grid to enable the presented Fourier analysis. The circular polarization of the laser was adjusted with a quarter-wave plate before the laser pulses were focused onto the sample in a normal-incidence geometry[49]. Dispersion introduced by transmissive optics and a vacuum window in the beam path was compensated using a pair of chirped mirrors (Venteon DCM7) and a pair of BK7 wedges (Newport FemtoOptics) by maximizing the electron emission signal in the microscope as a function of the wedge insertion.

The microscope is equipped with an imaging hemispherical energy filter, which provides an electron-optical energy resolution of typically <200 meV. It is, however, not sufficient to only consider the electron-optical resolution of the setup, but instead one needs to include the bandwidth of the SPP pulses that trigger the observed electron emission. The estimated SPP pulse duration of 15.8 fs (see discussion of the time-resolved data in Fig. 3) translates to a SPP pulse bandwidth of ≈120 meV. For 4th order electron emission we can thus estimate the combined energy resolution as $\sqrt{(200 \text{meV})^2 + 4 \cdot (120 \text{meV})^2} \approx 320$ meV, and for higher emission order the energy resolution scales accordingly.

Data Analysis

Calibration of plasmoemission spectroscopy data. While the imaging energy filter of the SPELEEM provides us with angle-resolved photoemission spectroscopy capabilities, its energy and momentum calibration depend on the instantaneous alignment of the microscope and need to be performed individually for each analyzed dataset. The momentum scale of the ARPLES data in Fig. 2 was calibrated by detecting the three-dimensional photoelectron horizon using an edge detection algorithm and fitting the detected edge using the free electron dispersion relation $E_{kin} = \hbar^2 k_\parallel^2 / 2m_e$, with m_e denoting the free electron mass. This fit was also used to correct for stigmatism related distortions of the momentum maps. Furthermore, the intrinsic linear nonisochromaticity of the energy filter in reciprocal space was corrected by cutting along slanted planes through the three-dimensional data. The typical S-shaped distortion of the line-like spectrum in the SPELEEM's dispersive plane was corrected by fitting a cubic polynomial to that S-shape and extracting the electron yield along this polynomial line. In all presented spectra, the photoelectron energy scale was calibrated by scanning the sample bias and tracking the linear shift of the respective spectrum. The offset between this energy scale and the final state energy scale was calibrated by fitting the point of inflection of the lowest order Fermi edge and attributing its energetic position to $E_{final} = E_F + 4\hbar\omega$ as discussed in the main text.

High dynamic range imaging. The used electron detector is operated in conjunction with dark current and flat-field corrections[71]. While these corrections greatly enhance the image quality and enable linear imaging, the comparably small signals from the high nonlinearities observed in this work are prone to remaining hot pixels. Hot pixels were identified by comparing the recorded images to median-filtered versions of these images. Subsequently, each identified hot pixel was corrected by replacing its value by the respective local median. To further increase the dynamic range of the electron detector, which is necessary for resolving the signals from the individual electron emission orders (data in Figs. 3 and 4) over several orders of magnitude, we employ a simple high-dynamic range reconstruction algorithm. At each delay step Δt we record a series of images $S_i(\Delta t)$ with varying exposure times t_i. The recorded images are clipped by choosing appropriate noise and saturation cutoffs and ignoring pixels outside of this range. For each delay step the images are then combined according to

$$\bar{S}(\Delta t) = \frac{\sum_i w_i S_i(\Delta t)/t_i}{\sum_i w_i}$$

to yield the averaged high-dynamic range signal $\bar{S}(\Delta t)$. The weights w_i are chosen assuming a linear detector response[75], such that $w_i = t_i^2$.

Data availability

All data needed to evaluate the conclusions in the paper are present in the paper and/or the Supplementary Materials. Additional data related to this paper are available from the corresponding authors upon request.

References

1. Basov, D. N., Averitt, R. D. & Hsieh, D. Towards properties on demand in quantum materials. *Nat. Mater.* **16**, 1077–1088 (2017).
2. Kruchinin, S. Y., Krausz, F. & Yakovlev, V. S. Colloquium: Strong-field phenomena in periodic systems. *Rev. Mod. Phys.* **90**, 21002 (2018).
3. de la Torre, A. et al. Colloquium: Nonthermal pathways to ultrafast control in quantum materials. *Rev. Mod. Phys.* **93**, 41002 (2021).
4. Shirley, J. H. Solution of the Schrödinger Equation with a Hamiltonian Periodic in Time. *Phys. Rev.* **138**, B979–B987 (1965).
5. Sambe, H. Steady States and Quasienergies of a Quantum-Mechanical System in an Oscillating Field. *Phys. Rev. A* **7**, 2203–2213 (1973).
6. Oka, T. & Kitamura, S. Floquet Engineering of Quantum Materials. *Annu. Rev. Condens. Matter Phys.* **10**, 387–408 (2019).
7. Rudner, M. S. & Lindner, N. H. Band structure engineering and non-equilibrium dynamics in Floquet topological insulators. *Nat. Rev. Phys.* **2**, 229–244 (2020).
8. Oka, T. & Aoki, H. Photovoltaic Hall effect in graphene. *Phys. Rev. B* **79**, 81406 (2009).
9. Lindner, N. H., Refael, G. & Galitski, V. Floquet topological insulator in semiconductor quantum wells. *Nat. Phys.* **7**, 490–495 (2011).
10. Holthaus, M. Floquet engineering with quasienergy bands of periodically driven optical lattices. *J. Phys. B* **49**, 13001 (2016).
11. Faisal, F. H. M. & Kamiński, J. Z. Floquet-Bloch theory of high-harmonic generation in periodic structures. *Phys. Rev. A* **56**, 748–762 (1997).
12. Eckardt, A. Colloquium: Atomic quantum gases in periodically driven optical lattices. *Rev. Mod. Phys.* **89**, 11004 (2017).
13. Hone, D. W., Ketzmerick, R. & Kohn, W. Statistical mechanics of Floquet systems: the pervasive problem of near degeneracies. *Phys. Rev. E* **79**, 051129 (2009).
14. Seetharam, K. I., Bardyn, C.-E., Lindner, N. H., Rudner, M. S. & Refael, G. Controlled Population of Floquet-Bloch States via Coupling to Bose and Fermi Baths. *Phys. Rev. X* **5**, 41050 (2015).
15. Aeschlimann, S. et al. Survival of Floquet-Bloch States in the Presence of Scattering. *Nano Lett.* **21**, 5028–5035 (2021).
16. Sato, S. A. et al. Floquet states in dissipative open quantum systems. *J. Phys. B* **53**, abb127 (2020).
17. Mahmood, F. et al. Selective scattering between Floquet–Bloch and Volkov states in a topological insulator. *Nat. Phys.* **12**, 306–310 (2016).
18. Wang, Y. H., Steinberg, H., Jarillo-Herrero, P. & Gedik, N. Observation of Floquet-Bloch states on the surface of a topological insulator. *Science* **342**, 453–457 (2013).
19. Reutzel, M., Li, A., Wang, Z. & Petek, H. Coherent multidimensional photoelectron spectroscopy of ultrafast quasiparticle dressing by light. *Nat. Commun.* **11**, 2230 (2020).
20. McIver, J. W. et al. Light-induced anomalous Hall effect in graphene. *Nat. Phys.* **16**, 38–41 (2020).
21. Atwater, H. A. The Promise of Plasmonics. *Sci. Am.* **296**, 56–62 (2007).
22. Davis, T. J. et al. Ultrafast vector imaging of plasmonic skyrmion dynamics with deep subwavelength resolution. *Science* **368**, eaba6415 (2020).
23. Dai, Y. et al. Plasmonic topological quasiparticle on the nanometre and femtosecond scales. *Nature* **588**, 616–619 (2020).
24. Barnes, W. L., Dereux, A. & Ebbesen, T. W. Surface plasmon subwavelength optics. *Nature* **424**, 824–830 (2003).
25. Dombi, P. et al. Strong-field nano-optics. *Rev. Mod. Phys.* **92**, 025003 (2020).
26. Bormann, R., Gulde, M., Weismann, A., Yalunin, S. V. & Ropers, C. Tip-enhanced strong-field photoemission. *Phys. Rev. Lett.* **105**, 147601 (2010).
27. Herink, G., Solli, D. R., Gulde, M. & Ropers, C. Field-driven photoemission from nanostructures quenches the quiver motion. *Nature* **483**, 190–193 (2012).
28. Dombi, P. et al. Ultrafast strong-field photoemission from plasmonic nanoparticles. *Nano Lett.* **13**, 674–678 (2013).
29. Podbiel, D. et al. Imaging the Nonlinear Plasmoemission Dynamics of Electrons from Strong Plasmonic Fields. *Nano Lett.* **17**, 6569–6574 (2017).
30. Schenk, M., Kruger, M. & Hommelhoff, P. Strong-field above-threshold photoemission from sharp metal tips. *Phys. Rev. Lett.* **105**, 257601 (2010).
31. Sivis, M. et al. Continuous-wave multiphoton photoemission from plasmonic nanostars. *Commun. Phys.* **1**, 13 (2018).
32. Han, S. et al. High-harmonic generation by field enhanced femtosecond pulses in metal-sapphire nanostructure. *Nat. Commun.* **7**, 13105 (2016).
33. Ropers, C. et al. Grating-coupling of surface plasmons onto metallic tips: a nanoconfined light source. *Nano Lett.* **7**, 2784–2788 (2007).
34. Neacsu, C. C. et al. Near-field localization in plasmonic superfocusing: a nanoemitter on a tip. *Nano Lett.* **10**, 592–596 (2010).
35. Schmidt, S. et al. Adiabatic nanofocusing on ultrasmooth single-crystalline gold tapers creates a 10-nm-sized light source with few-cycle time resolution. *ACS Nano* **6**, 6040–6048 (2012).
36. Berweger, S., Atkin, J. M., Xu, X. G., Olmon, R. L. & Raschke, M. B. Femtosecond nanofocusing with full optical waveform control. *Nano Lett.* **11**, 4309–4313 (2011).
37. Podbiel, D. et al. Spatiotemporal Analysis of an Efficient Fresnel Grating Coupler for Focusing Surface Plasmon Polaritons. *ACS Photonics* **6**, 600–604 (2019).
38. Liu, Z. et al. Focusing surface plasmons with a plasmonic lens. *Nano Lett.* **5**, 1726–1729 (2005).
39. Frank, B. et al. Short-range surface plasmonics: Localized electron emission dynamics from a 60-nm spot on an atomically flat single-crystalline gold surface. *Sci. Adv.* **3**, e1700721 (2017).
40. Spektor, G., David, A., Gjonaj, B., Bartal, G. & Orenstein, M. Metafocusing by a Metaspiral Plasmonic Lens. *Nano Lett.* **15**, 5739–5743 (2015).
41. Gorodetski, Y., Niv, A., Kleiner, V. & Hasman, E. Observation of the spin-based plasmonic effect in nanoscale structures. *Phys. Rev. Lett.* **101**, 043903 (2008).
42. Spektor, G. et al. Revealing the subfemtosecond dynamics of orbital angular momentum in nanoplasmonic vortices. *Science* **355**, 1187–1191 (2017).
43. Kim, H. et al. Synthesis and dynamic switching of surface plasmon vortices with plasmonic vortex lens. *Nano Lett.* **10**, 529–536 (2010).
44. Reutzel, M., Li, A. & Petek, H. Coherent Two-Dimensional Multiphoton Photoelectron Spectroscopy of Metal Surfaces. *Phys. Rev. X* **9**, 011044 (2019).
45. Schmidt, T. et al. SPELEEM: Combining LEEM and Spectroscopic Imaging. *Surf. Rev. Lett.* **05**, 1287–1296 (1998).
46. Radha, B., Arif, M., Datta, R., Kundu, T. K. & Kulkarni, G. U. Movable Au microplates as fluorescence enhancing substrates for live cells. *Nano Res* **3**, 738–747 (2010).
47. Radha, B. & Kulkarni, G. U. A Real Time Microscopy Study of the Growth of Giant Au Microplates. *Cryst. Growth Des.* **11**, 320–327 (2011).
48. Barth, J. V., Brune, H., Ertl, G. & Behm, R. J. Scanning tunneling microscopy observations on the reconstructed Au(111) surface: Atomic structure, long-range superstructure, rotational domains, and surface defects. *Phys. Rev. B* **42**, 9307–9318 (1990).
49. Kahl, P. et al. Normal-Incidence Photoemission Electron Microscopy (NI-PEEM) for Imaging Surface Plasmon Polaritons. *Plasmonics* **9**, 1401–1407 (2014).
50. Meyer zu Heringdorf, F.-J. et al. Signatures of plasmoemission in two photon photoemission electron microscopy. *Proc. SPIE* **9361**, 93610V (2015).
51. Davis, T. J. et al. Subfemtosecond and Nanometer Plasmon Dynamics with Photoelectron Microscopy: Theory and Efficient Simulations. *ACS Photonics* **4**, 2461–2469 (2017).
52. Derry, G. N., Kern, M. E. & Worth, E. H. Recommended values of clean metal surface work functions. *J. Vac. Sci. Technol. A* **33**, 060801 (2015).
53. Yan, B. et al. Topological states on the gold surface. *Nat. Commun.* **6**, 10167 (2015).
54. Kevan, S. D. & Gaylord, R. H. High-resolution photoemission study of the electronic structure of the noble-metal (111) surfaces. *Phys. Rev. B* **36**, 5809–5818 (1987).
55. Reinert, F., Nicolay, G., Schmidt, S., Ehm, D. & Hüfner, S. Direct measurements of the L-gap surface states on the (111) face of noble metals by photoelectron spectroscopy. *Phys. Rev. B* **63**, 115415 (2001).
56. Li, A. et al. Towards full surface Brillouin zone mapping by coherent multi-photon photoemission. *New J. Phys.* **22**, ab98d6 (2020).
57. Reutzel, M., Li, A. & Petek, H. Above-threshold multiphoton photoemission from noble metal surfaces. *Phys. Rev. B* **101**, 75409 (2020).
58. Li, A. D. et al. Plasmonic Photoemission from Single-Crystalline Silver. *ACS Photonics* **8**, 247–258 (2021).
59. Reutzel, M., Li, A., Gumhalter, B. & Petek, H. Nonlinear Plasmonic Photoelectron Response of Ag(111). *Phys. Rev. Lett.* **123**, 017404 (2019).
60. Tromp, R. M. et al. A simple energy filter for low energy electron microscopy/photoelectron emission microscopy instruments. *J. Phys. Condens. Matter* **21**, 314007 (2009).
61. Yanagisawa, H. et al. Delayed electron emission in strong-field driven tunnelling from a metallic nanotip in the multi-electron regime. *Sci. Rep.* **6**, 35877 (2016).
62. Petek, H. & Ogawa, S. Femtosecond time-resolved two-photon photoemission studies of electron dynamics in metals. *Prog. Surf. Sci.* **56**, 239–310 (1997).
63. Bauer, M., Marienfeld, A. & Aeschlimann, M. Hot electron lifetimes in metals probed by time-resolved two-photon photoemission. *Prog. Surf. Sci.* **90**, 319–376 (2015).
64. Steeb, F. et al. The nature of a nonlinear excitation pathway from the Shockley surface state as probed by chirped pulse two photon photoemission. *New J. Phys.* **11**, 13016 (2009).

65. Stibenz, G. & Steinmeyer, G. Interferometric frequency-resolved optical gating. *Opt. Express* **13**, 2617–2626 (2005).

66. Zhong, J. H. et al. Nonlinear plasmon-exciton coupling enhances sum-frequency generation from a hybrid metal/semiconductor nanostructure. *Nat. Commun.* **11**, 1464 (2020).

67. Sirotti, F. et al. Multiphoton k-resolved photoemission from gold surface states with 800-nm femtosecond laser pulses. *Phys. Rev. B* **90**, 35401 (2014).

68. Venuthurumilli, P. K., Wen, X., Iyer, V., Chen, Y. P. & Xu, X. Near-Field Imaging of Surface Plasmons from the Bulk and Surface State of Topological Insulator Bi2Te2Se. *ACS Photonics* **6**, 2492–2498 (2019).

69. Hu, F. et al. Imaging exciton–polariton transport in MoSe2 waveguides. *Nat. Photonics* **11**, 356–360 (2017).

70. Dai, S. et al. Tunable phonon polaritons in atomically thin van der Waals crystals of boron nitride. *Science* **343**, 1125–1129 (2014).

71. Janoschka, D. et al. Implementation and operation of a fiber-coupled CMOS detector in a low energy electron Microscope. *Ultramicroscopy* **221**, 113180 (2020).

72. Da Browski, M., Dai, Y. & Petek, H. Ultrafast Photoemission Electron Microscopy: Imaging Plasmons in Space and Time. *Chem. Rev.* **120**, 6247–6287 (2020).

73. Wehner, M. U., Ulm, M. H. & Wegener, M. Scanning interferometer stabilized by use of Pancharatnam's phase. *Opt. Lett.* **22**, 1455–1457 (1997).

74. Meyer zu Heringdorf, F. J. et al. Spatio-temporal imaging of surface plasmon polaritons in two photon photoemission microscopy. *Proc. SPIE* **9921**, 992110 (2016).

75. Robertson, M. A. Estimation-theoretic approach to dynamic range enhancement using multiple exposures. *J. Electr. Imag.* **12**, 1557695 (2003).

Author contributions
P.D., D.J., and F.-J.MzH. performed the experiments. P.D. performed the data analysis. B.F. fabricated the samples. P.D., D.J., B.F., H.G., and F.-J.MzH. contributed to the data interpretation and discussions. The manuscript was written through contributions of all authors.

Competing interests
The authors declare no competing interests.

Additional information
Supplementary information The online version contains supplementary material available at https://doi.org/10.1038/s42005-023-01128-w.

Correspondence and requests for materials should be addressed to Pascal Dreher.

Peer review information *Communications Physics* thanks the anonymous reviewers for their contribution to the peer review of this work.

Reprints and permission information is available at http://www.nature.com/reprints

Publisher's note Springer Nature remains neutral with regard to jurisdictional claims in published maps and institutional affiliations.

DuEPublico

Duisburg-Essen Publications online

UNIVERSITÄT
DUISBURG
ESSEN

Offen im Denken

ub | universitäts
bibliothek